# Effect of Rare Earth on the Corrosion Resistance of Electroless Ni-Mo-P Composite Coatings

*Ya-Peng Jia[a]* (ID)*, Wan-Chang Sun[a]\** (ID)*, Yan Xiao[a]* (ID)*, Yu-Wan Liu[a]* (ID)*, Sha-Sha Tian[a]* (ID)

[a]*Xi'an University of Science and Technology, College of Materials Science and Engineering, Xi'an, Shaanxi, 710054, China.*

A kind of corrosion-resistant Ni-Mo-P composite coating was deposited on the surface of AZ91D magnesium alloy substrate by electroless plating method with different concentration of $Ce(NO_3)_3$ and $Nd(NO_3)_3$. The deposition mechanism of Ni-Mo-P composite coating was explored. Furthermore, the effects of $Ce(NO_3)_3$ and $Nd(NO_3)_3$ concentration on the microstructure and properties of Ni-Mo-P composite coatings were studied. Results indicated that the Ni-Mo-P composite coatings prepared by adding the optimal concentration of $Ce(NO_3)_3$ and $Nd(NO_3)_3$ had few defects. Meanwhile, the deposition rate of the composite coatings and the adhesion between the coating and the magnesium alloy substrate were improved. When the concentration of $Ce(NO_3)_3$ and $Nd(NO_3)_3$ were 0.10 and 1.00 g/L, the Ni-Mo-P composite coatings had the minimum corrosion rate of 0.826 and 0.681 $g/m^2 \cdot h$, respectively. Herein, compared with the addition of $Ce(NO_3)_3$, the $Nd(NO_3)_3$ added Ni-Mo-P composite coating has the maximum arc radius of capacitive resistance and significant improvement corrosion resistance.

**Keywords:** *AZ91D magnesium alloy, Electroless plating, Ni-Mo-P composite coatings, Rare earth, Microstructure, Corrosion resistance.*

## 1. Introduction

Magnesium alloys are potentially applied in aerospace, automotive, electronics and biomedical applications due to light weight, low density, high strength, and excellent recyclability[1-4]. However, high chemical reactivity of magnesium alloys is susceptible to corrosion and wear resistance, which hinders its widespread development[5-7]. Therefore, numerous surface modification techniques such as chemical transformation[8], microarc oxidation[9], chemical vapor depositions[10], Electrodeposition[11,12] and electroless plating[13] are presented for obtaining corrosion resistant coatings on magnesium alloys.

Electroless Ni-P coating is considered as the preferred method among various surface treatments to enhance the corrosion and wear resistance of magnesium alloys[14-16]. Recently, for exploring the application of electroless Ni-P coating, co-deposition of metallic elements such as W[17,18], Cu[19], Ag[20], Fe[21], Zn[22], Mo[23], and Co[24] formed Ni-X-P ternary alloy coatings with superior hardness, corrosion resistance and wear resistance. In particular, the Ni-W-P coating have received wide attention due to the special characteristics of the W element, such as high hardness, high melting point and low coefficient of expansion[25]. Ni-Mo-P coating offers better thermal stability, wear resistance and corrosion resistance than Ni-W-P coating since Mo was added to the Ni-P coating for high temperature and antioxidant[26].

On the other hand, the rare earth elements (RE) were reported as a typically industrial monosodium glutamate to modulate the corrosion resistance of Mg. Such as Ce, Nd, Y and La based on their unique electronic layer structure[27-29]. Ce and Nd elements can be introduced into the plating solution to improve the corrosion resistance of AZ91D magnesium alloy without any deterioration in their mechanical properties[30-32]. However, the study about the corrosion resistance of Ni-Mo-P composite coating with Ce and Nd elements on the surface of AZ91D magnesium alloy has been seldom reported.

In this paper, the Ni-Mo-P composite coatings with different $Ce(NO_3)_3$ and $Nd(NO_3)_3$ concentration was prepared by electroless plating and special pretreatment on magnesium alloy substrate, aiming to improve the corrosion resistance of magnesium alloys. The microstructures, phase composition, deposition rate, corrosion resistance and adhesion between the coating and the substrate of Ni-Mo-P composite coatings with different concentration of $Ce(NO_3)_3$ and $Nd(NO_3)_3$ were studied. Furthermore, the deposition mechanism of Ni-Mo-P composite coating was explored.

## 2. Experimental Methods

### 2.1. Pretreatments

AZ91D magnesium alloy substrate with a size of 16mm×10mm×8mm were polished with abrasive paper of successively finer grit down to 2,000 grit in order to remove oxides. Thereafter, the substrates were cleaned by ultrasonic shock degreasing in acetone for 15 min and washed with distilled water.

In order to promote the corrosion resistance, denseness and adhesion between the coating and the substrate of Ni-

Mo-P composite coating, an appropriate pretreatment process would be essential before electroless plating of AZ91D magnesium alloys. The main parameters and techniques of pretreatment are presented in Table 1. The samples were washed with distilled water and air dried, then electroless plated in plating baths containing 0.05-0.20 g/L $Ce(NO_3)_3$ or 0.5-1.50 g/L $Nd(NO_3)_3$. The electroless bath composition and processing parameters are shown in Table 2. During the experiments, all solutions were prepared using analytical reagents and deionized water, Furthermore, the bath temperature was maintained at the desired value by using thermostatic water bath.

## 2.2. Characterization

The microscopic morphology (cross-sectional morphology and surface morphology) of Ni-Mo-P composite coating was analyzed by scanning electron microscope (SEM, JSM-6390A, Japan), and the composition of coating was determined by the energy dispersive spectroscopy (EDS) equipped with SEM.The phase structure of the coating was characterized by X-ray diffractometer (XRD-7000, Shimadzu, Japan) with a Cu Kα radiation (Kα=0.15406 nm) in the 2θ range of 20°~80°. The deposition rate of the coating is calculated from the ratio of the coating weight to the product of the deposition time and the surface area of the coating. WS-2005 automatic scratch tester was adopted to evaluate the adhesion strength of Ni-Mo-P composite coating for the critical load. During the test, the specimen was loaded from a load of 0.1 N to 50 N at a loading rate of 20 N/min with the scratch length of 3 mm.

## 2.3. Corrosion resistance testing of Ni-Mo-P composite coatings

The Corrosion resistance of Ni-Mo-P composite coating was examined by corrosion immersion test and electrochemical test. The samples with exposed surface area of 10 mm x 10 mm were immersed in 3.5 wt.% NaCl solution for 72 h under standard temperature and pressure, before they were sealed in the mixture of rosin and paraffin.

Electrochemical Impedance Spectroscopy (EIS) is an electrical measurement method which adopts amplitude sine wave potential as the interference signal. The initial use of frequency response analysis within the range of 0.01 Hz-0.1 MHz with amplitude of 10 mV was designed to protect the integrity of the specimen. The dynamic potential polarization curve at the rate of 0.333 mV/s, the scanning range was ±250 mV as well the scanning time of 30 min was demonstrated. The experimental setup is shown in Fig. 1.

**Table 1.** The parameters and operating conditions of pretreatment.

| Process operation | Solution composition | Concentration | Conditions |
|---|---|---|---|
| Alkaline | NaOH | 60 g/L | 60~70°C<br>8~15 min<br>Magnetic agitation |
| | $Na_3PO_4$ | 10 g/L | |
| Pickling | $H_3PO_4$ | 30 mL/L | 25°C<br>10~20s |
| | KF | 15 g/L | |
| Activation | HF | 370 ml/L | 25°C<br>10 min |
| | NaF | 20 g/L | |
| Zinc dip | $ZnSO_4$ | 30 g/L | 80°C<br>5 min<br>Magnetic agitation |
| | $Na_4P_2O_7$ | 120 g/L | |
| | KF | 7 g/L | |
| | $Na_2CO_4$ | 5 g/L | |
| De-zincification | $HNO_3$ | 100 mL/L | 5-15 s<br>Room temperature |
| Secondary dip zinc | Same as zinc dip | | 80°C<br>2 min<br>Magnetic agitation |

**Table 2.** The electroless bath composition and processing parameters for electroless plating.

| Bath composition | Concentration / (g·L$^{-1}$) | Operating conditions |
|---|---|---|
| $NiSO_4 \cdot 6H_2O$ | 20 | |
| $NaH_2PO_2$ | 30 | |
| $Na_3C_6H_5O_7$ | 40 | |
| $CH_3COONa$ | 12 | Temperature: 85°C<br>Plating time: 1.5 h<br>Bath pH: 9.2-9.7<br>Agitation speed: 300 r/min |
| NaF | 0.7 | |
| $Na_2MoO_4$ | 1 | |
| $Ce(NO_3)_3$ | 0~0.2 | |
| $Nd(NO_3)_3$ | 0.5~1.5 | |

# 3. Results and Discussion

## 3.1. Deposition mechanism

The deposition mechanism of the Ni-Mo-P composite coating is illustrated in Fig. 2. At the beginning of electroless plating, the chemically active reducing agent $H_2PO_2^-$ hydrolyzes to produce $H_2PO_3^-$, $H^+$ and hydrogen atoms [H]. The autocatalytic reaction in the plating solution is initially weak. $Ni^{2+}$ is reduced to metallic nickel by some [H], and part of [H] reduces $H_2PO_2^-$, precipitating phosphorus atoms deposited on the nickel surface. The reduction of nickel induces the co-deposition of elemental molybdenum with

nickel phosphorus, and $MoO_4^{2-}$ is reduced to molybdenum atoms by [H]. Finally, the complete Ni-Mo-P composite coating is formed on the surface of magnesium alloy. During deposition, the $Ce^{3+}$ or $Nd^{3+}$ in the plating solution accelerates the reduction rate of Ni and Mo atoms by adsorption on the metal surface, which reduces the energy of the system. The electrode potential of the reducing agent is much higher than that of $Ce(NO_3)_3$ and $Nd(NO_3)_3$, therefore it is difficult to occur the redox reaction between $Ce^{3+}$ or $Nd^{3+}$ and the reducing agent, which causes them not to change the deposition pattern of Ni-Mo-P coating. In addition, the [H] in the solvation cell combines to precipitate hydrogen gas, producing small bubbles during the reaction. It is worth noted that the reduction of molybdenum and phosphorus atoms have a mutually constraining relationship due to the limited amount of [H] produced by the hydrolysis of $H_2PO_2^-$ in the plating solution. The relationship equation of the reaction is:

$$H_2PO_2^- + H_2O \rightarrow HPO_3^- + H^+ + 2[H] \tag{3.1}$$

$$Ni^{2+} + 2[H] \rightarrow Ni + 2H^+ \tag{3.2}$$

$$H_2PO_2^- + [H] \rightarrow H_2O + OH^- + P \tag{3.3}$$

$$MoO_4^{2-} + 6[H] \rightarrow Mo + 2OH^- + 2H_2O \tag{3.4}$$

$$2[H] \rightarrow H_2 \uparrow \tag{3.5}$$
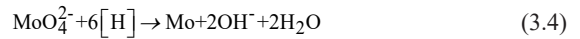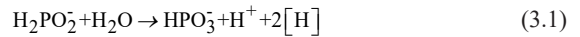
## 3.2. Cross-sectional morphology and composition of Ni-Mo-P composite coatings

In order to observe the bonding of Ni-Mo-P composite coating with the magnesium alloy substrate, which the cross-sectional morphology and line EDS are discussed in Fig. 3. As can be seen from Fig. 3 (a) and (b), the dark gray area is the magnesium alloy substrate and the light gray area is the Ni-Mo-P composite coating, indicating that the Ni-Mo-P composite coating was successfully prepared on the surface of the bare substrate by electroless. Theoretically, there is a
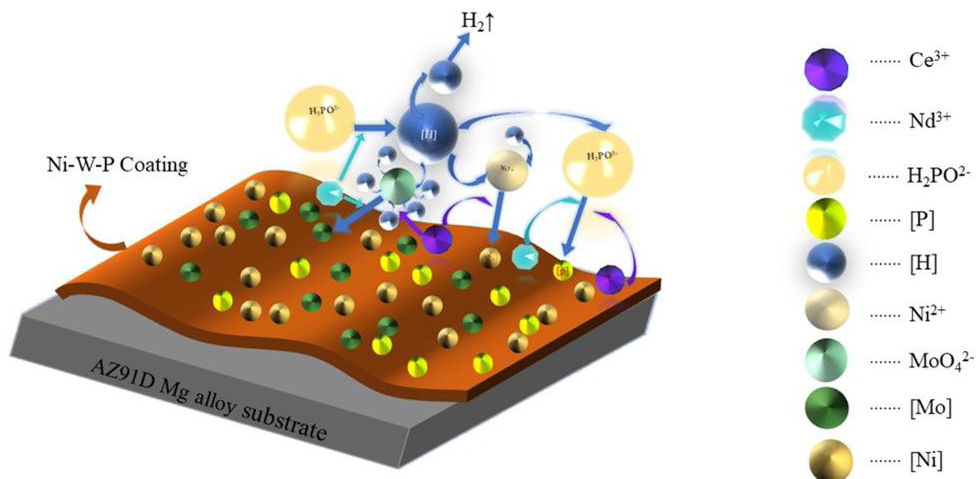


**Figure 1.** Schematic diagram of electrochemical test equipment.



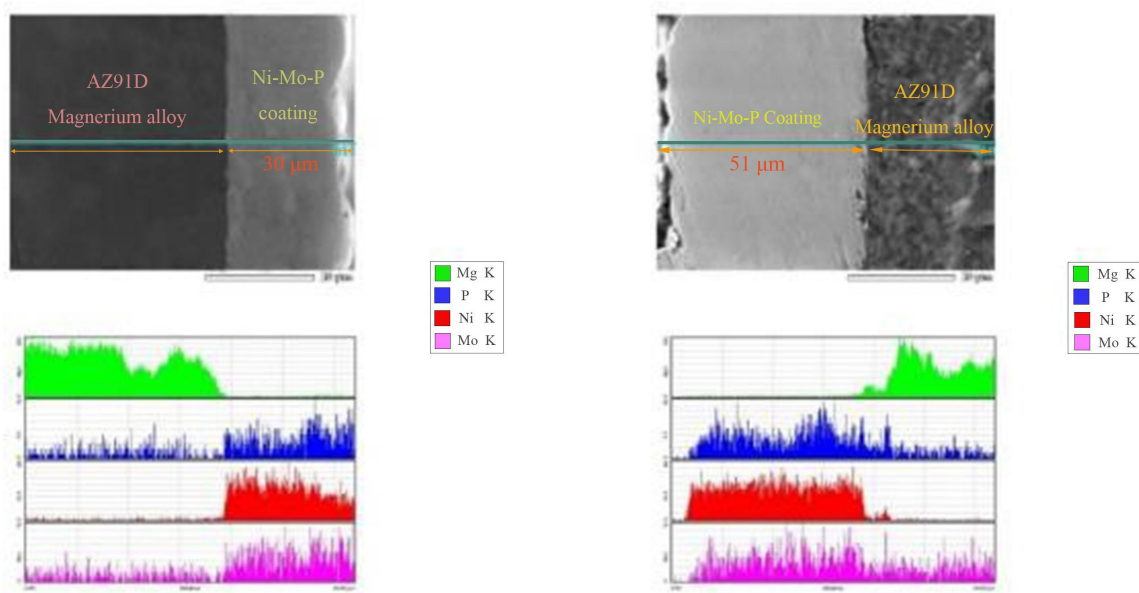**Figure 2.** Schematic diagram of the deposition mechanism of Ni-Mo-P composite coating.

**Figure 3.** The cross-sectional morphology and line EDS of Ni-Mo-P composite coatings (a) 0.10 g/L Ce(NO$_3$)$_3$ (b) 1.00 g/L Nd(NO$_3$)$_3$.

metal layer formed during zinc dipping between the coating and the substrate. Nevertheless, the zinc layer is too thin to be viewed immediately. Simultaneously, the thickness of Ni-Mo-P composite coating with Nd(NO$_3$)$_3$ added at 1.00 g/L is about 51 μm, which is better than that of Ni-Mo-P composite coating with Ce(NO$_3$)$_3$ added at 0.10 g/L. With the addition of Ce(NO$_3$)$_3$ at 0.10 g/L, the Ni-Mo-P coating thickness is about 30 μm. That is because, compared with cerium ions, neodymium ions have a larger nuclear charge, which can better promote the adsorption of metal ligand ions and reductant ions to the surface for magnesium alloy. Meanwhile, it provides catalytic activity for the nucleation of the alloy, which results in better nucleation and better deposition rate.

### 3.3. Surface morphologies and composition of Ni-Mo-P composite coatings

The surface morphologies of the Ni-Mo-P composite coatings by electroless plating under different Ce(NO$_3$)$_3$ concentration are illustrated in Fig. 4. As far as we know, the composite coatings with dense structure represent superior performance. By comparing Fig. 4 (a-e), it can be noted that the cellular organization of the surface morphologies of the coatings are larger and less dense when the concentration of Ce(NO$_3$)$_3$ is 0 g/L, 0.05 g/L and 0.2 g/L. It is clear that when the concentration of Ce(NO$_3$)$_3$ is 0.10 g/L, the cellular organization of the coating is minimal and the coating is smooth as well as dense.

Based on the EDS results of Ni-Mo-P composite coatings with different Ce(NO$_3$)$_3$ concentration are depicted in Fig. 5 (a-e). Found that the main components of the composite coatings are composed of Ni, Mo and P elements. The mass percentages of elements in the Ni-Mo-P composite coatings are listed in Table 3. As the concentration of Ce(NO$_3$)$_3$ in the plating solution increases, the percentage of P in the composite coatings increases and then decreases, while the

**Table 3.** Results of energy spectrum analysis of Ni-Mo-P composite coatings.

| Ce(NO$_3$)$_3$(g/L) | Ni(wt.%) | P(wt.%) | Mo(wt.%) |
|---|---|---|---|
| 0 | 85.30 | 7.57 | 7.13 |
| 0.05 | 84.75 | 8.79 | 6.46 |
| 0.10 | 88.16 | 10.12 | 1.72 |
| 0.15 | 85.98 | 9.45 | 4.57 |
| 0.20 | 85.31 | 8.47 | 6.22 |

percentage of Mo decreases and then increases. The results show that the addition of appropriate Mo can promote the deposition reaction of P, increasing the mass fraction of P in the Ni-Mo-P composite coating. In addition, when the concentration of Ce(NO$_3$)$_3$ is 0.10 g/L and 0.15 g/L, the mass fraction of P in the composite coating are more than 9%, so both Ni-Mo-P composite coatings are amorphous structures. While the composite coatings of the other samples with P mass fractions between 7% and 9% are microcrystalline structures.

Fig. 6 shows the surface morpholoies of the Ni-Mo-P composite coatings by electroless plating under different Nd(NO$_3$)$_3$ concentration. From Fig. 6 (a-e), without the surface defects of leakage plating. The morphological surfaces of the Ni-Mo-P composite coatings with 0.75 g/L, 1.00 g/L and 1.25 g/L concentration are both dense and homogeneous. Furthermore, there are significant agglomeration phenomenon, which ensuring reliable corrosion resistance of the coating. Indicating that the adopted previously surface pretreatment method can achieve better nickel-based coatings on magnesium alloy. The cellular organization of the composite coatings became decreasing and then increasing with the increasing concentration of Nd(NO$_3$)$_3$, which may be caused by the change of the mass fraction of Mo in the Ni-Mo-P composite coatings.The optimal coating is obtained when the Nd(NO$_3$)$_3$ concentration is 1.00 g/L.
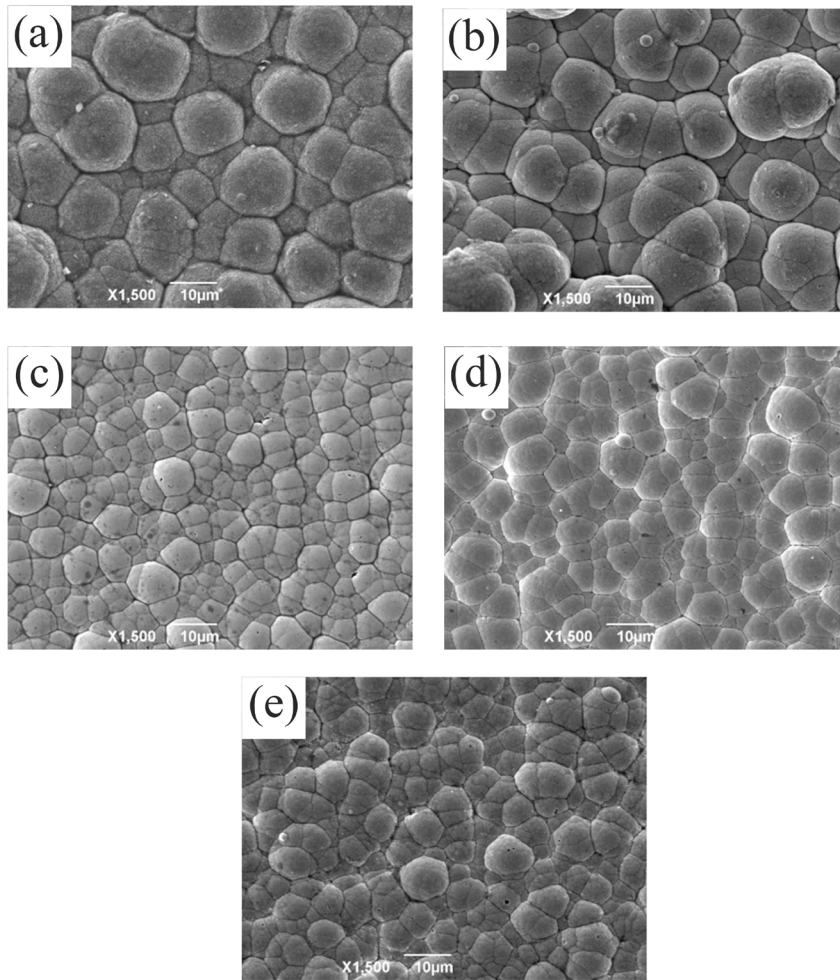
**Figure 4.** The surface morphologies of Ni-Mo-P composite coatings with different Ce(NO$_3$)$_3$ concentration (a) 0 g/L (b) 0.05 g/L (c) 0.10 g/L (d) 0.15 g/L (e) 0.20 g/L.

Fig. 7 (a-e) displays that the EDS results of the Ni-Mo-P composite coatings with different Nd(NO$_3$)$_3$ concentration and the data from the energy spectrum analysis are listed in Table 4. It is evident that when the concentration of Nd(NO$_3$)$_3$ is increases from 0.50 g/L to 1.00 g/L, the mass percentage of Mo reduces from 7.29% to 1.57%, while the mass percentage of P improves from 8.34% to the maximum value of 10.78% which results to the highest amorphous degree of coating. Meanwhile, the Ni-Mo-P composite coatings with concentration of 0.75 g/L, 1.00 g/L, 1.25 g/L and 1.50 g/L are all amorphous structures, except for the Nd(NO$_3$)$_3$ concentration which is 0.50 g/L and clarified that the amorphization of the Ni-Mo-P composite coatings would promote by adding appropriate content of Nd(NO$_3$)$_3$.

### 3.4. Effect of Ce(NO$_3$)$_3$ and Nd(NO$_3$)$_3$ concentration on phase composition and deposition rate of Ni-Mo-P coatings

The XRD patterns of Ni-Mo-P composite coatings are presented in Fig. 8. Observing Fig. 8 (a-e), the diffraction peak of the Ni-Mo-P composite coating the Ni (111) plane (2θ=45°) is slightly sharp, implying it shows the microcrystalline structure, which is caused by the entry of P atoms into the face-centered cubic Ni lattice, destroying the crystalline structure of Ni. In contrast, the diffraction peaks of the composite coatings with Ce(NO$_3$)$_3$ and Nd(NO$_3$)$_3$ are relatively lower intensity and wider width, which have typical amorphous structures. The composite coating with Nd(NO$_3$)$_3$ concentration of 1.00 g/L has the most wide diffraction peaks, higher P content and the best degree of amorphization. The amorphous structure has relatively tight structure and superior corrosion resistance due to the grain boundaries are not obvious. Hence, the addition of Nd(NO$_3$)$_3$ to the plating solution exhibits higher corrosion resistance compared to the addition of Ce(NO$_3$)$_3$.

The effect of the variation of Ce(NO$_3$)$_3$ and Nd(NO$_3$)$_3$ concentration on the deposition rate in this experiment are demonstrated in Fig. 9. The deposition rate increasing with increasing Ce(NO$_3$)$_3$ concentration, when the concentration is below 0.10 g/L. In particular, when the Ce(NO$_3$)$_3$ concentration is 0.10 g/L, the deposition rate of the composite coating is about 28.35 mg/dm$^2$·h, reaching the fastest. As the Ce(NO$_3$)$_3$ concentration increased again, the deposition rate shows a decreasing trend. The result

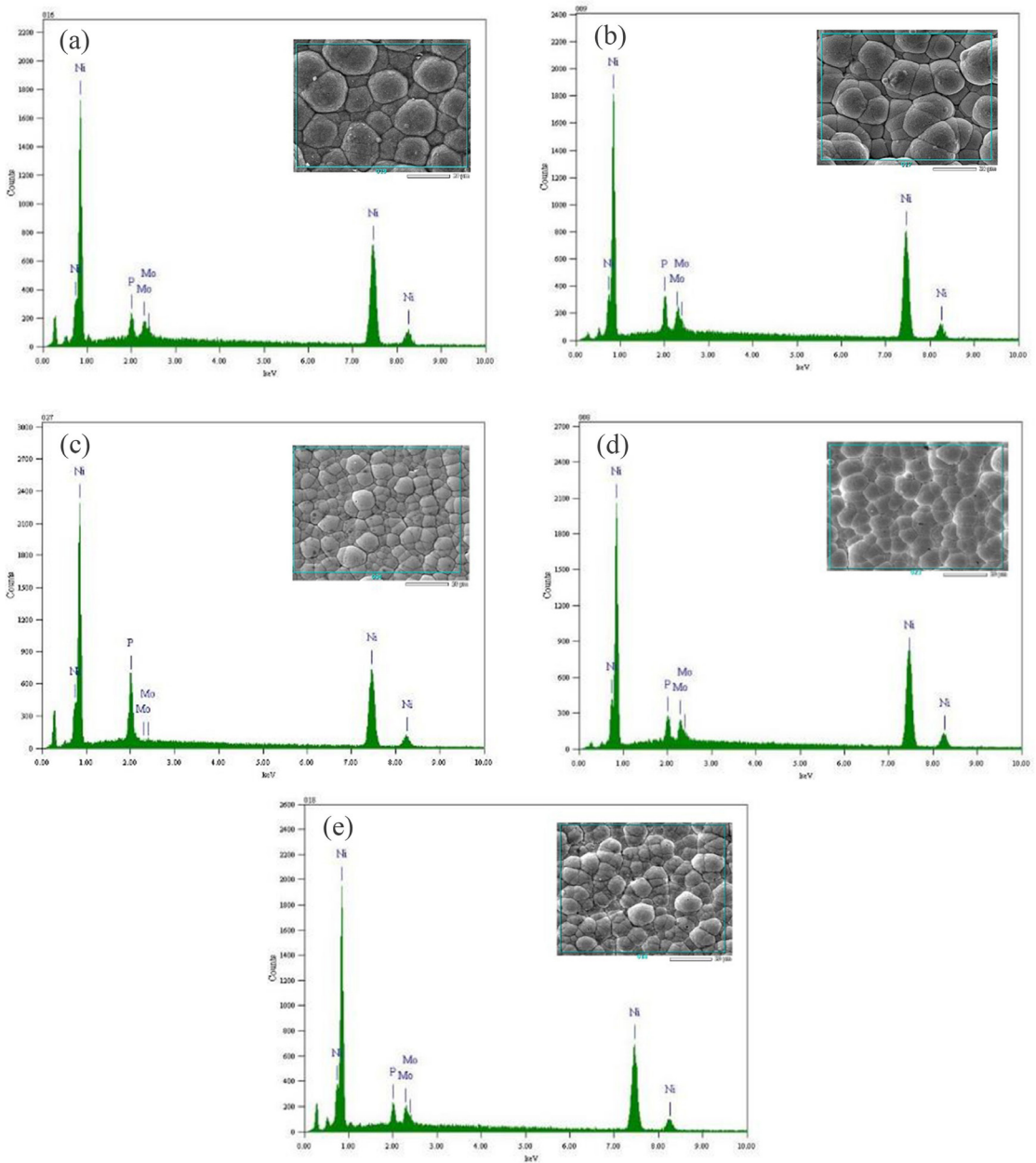**Figure 5.** EDS spectra of Ni-Mo-P composite coatings with different $Ce(NO_3)_3$ concentration (a) 0 g/L (b) 0.05 g/L (c) 0.10 g/L (d) 0.15 g/L (e) 0.20 g/L.

**Table 4.** Results of energy spectrum analysis of Ni-Mo-P composite coatings.

| $Nd(NO_3)_3$(g/L) | Ni(wt.%) | P(wt.%) | Mo(wt.%) |
|:---:|:---:|:---:|:---:|
| 0.50 | 84.37 | 8.34 | 7.29 |
| 0.75 | 84.63 | 9.02 | 6.35 |
| 1.00 | 87.65 | 10.78 | 1.57 |
| 1.25 | 88.19 | 9.63 | 2.18 |
| 1.50 | 84.09 | 9.17 | 6.74 |

is shown in Fig. 9 (a). Fig. 8 (b) shows that the effect of $Nd(NO_3)_3$ and $Ce(NO_3)_3$ concentrations on the deposition rate of the composite coatings has the same trend. When the concentration of $Nd(NO_3)_3$ is 1.00 g/L, the deposition rate

reaches the maximum value of about 30.28 mg/dm²·h. The analysis clarifies that the deposition rate of the composite coatings can be improved by increasing the concentration of $Ce(NO_3)_3$ and $Nd(NO_3)_3$ in the range of the lower
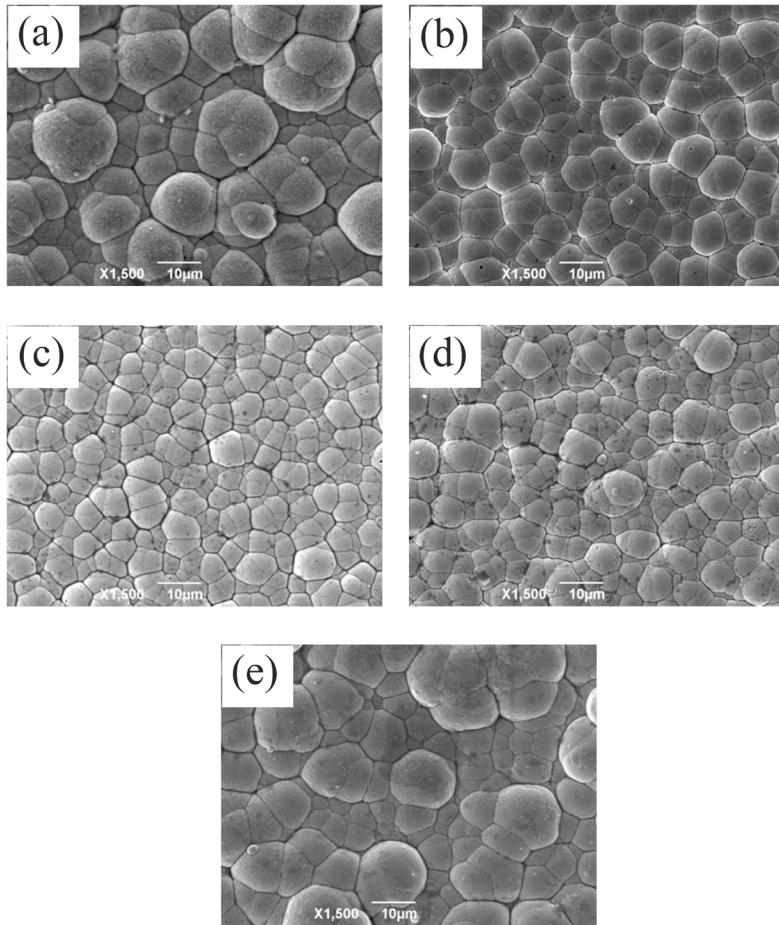
**Figure 6.** The surface morphologies of the Ni-Mo-P composite coatings with different concentration of $Nd(NO_3)_3$ (a) 0.50 g/L (b) 0.75 g/L (c) 1.00 g/L (d) 1.25 g/L (e) 1.50 g/L.

concentration, as well as the addition of $Nd(NO_3)_3$ is more effective towards the improvement to the deposition rate of the composite coatings.

## 3.5. Effect of $Ce(NO_3)_3$ and $Nd(NO_3)_3$ concentration on the adhesion strength

Combination strength of the Ni-Mo-P composite coatings and magnesium substrate is characterized by critical load. Fig. 10 presents the curve of the acoustic emission signal-pressure loading (K-L) of the composite coatings with different $Ce(NO_3)_3$ concentration. The critical load of the Ni-Mo-P composite coating is observed to be the minimum, about 35.00 N. With the increase of $Ce(NO_3)_3$ concentration in the plating solution, the critical load value of the composite coatings gradually increases and then decreases. When the concentration of $Ce(NO_3)_3$ in the plating solution is 0.10 g/L, the combination between the composite coating and the substrate becomes the optimum, which means the pressure loading load increases to 43.05 N, the acoustic emission intensity suddenly increases and the composite coating begins to peel and flake off.

The relationship curves between acoustic emission signal and pressure loading load for the composite coatings with

different $Nd(NO_3)_3$ concentration are shown in Fig. 11. From the chart, when the concentration of $Nd(NO_3)_3$ in the plating solution is lower, with the increase of $Nd(NO_3)_3$ content, the combination strength between the composite coatings and the metal increases, but the increase gradually reduces. The optimal combination parameter between the coating and the substrate at the $Nd(NO_3)_3$ concentration of 1.00 g/L is 48 N. It shows that the combination strength between the Ni-Mo-P composite coatings and substrate can be improved by adding $Nd(NO_3)_3$ and $Ce(NO_3)_3$ in the plating solution, for the addition of $Nd(NO_3)_3$ and $Ce(NO_3)_3$ will promote the amorphization level of the composite coatings, making the composite coatings smooth and dense.

## 3.6. Corrosion resistance of Ni-Mo-P composite coatings

### 3.6.1. Effect of $Ce(NO_3)_3$ and $Nd(NO_3)_3$ concentration on the corrosion rate of Ni-Mo-P composite coatings

The corrosion rates of the Ni-Mo-P composite coatings prepared at different $Ce(NO_3)_3$ and $Nd(NO_3)_3$ concentration are presented in Fig. 12 (a) and (b).That is evident in Fig. 12 (a), as the concentration of $Ce(NO_3)_3$ increases to 0.10 g/L, the
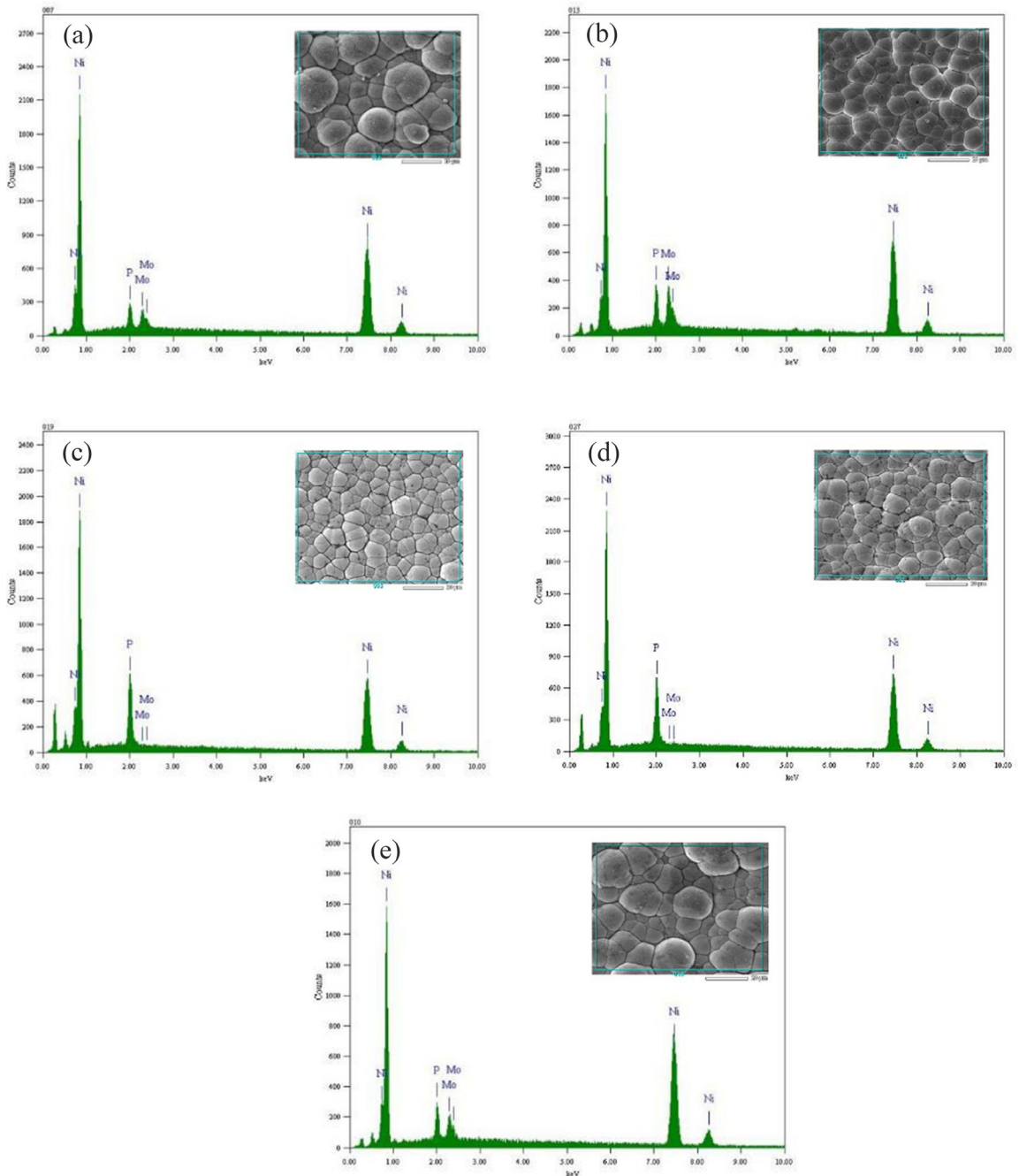
**Figure 7.** EDS spectra of the Ni-Mo-P composite coatings with different $Nd(NO_3)_3$ concentration (a) 0.50 g/L (b) 0.75 g/L (c) 1.00 g/L (d) 1.25 g/L (e) 1.50 g/L.

corrosion rate of the composite coatings rapidly decreases to the lowest point of 0.826 $g/m^2 \cdot h$, and the corrosion resistance of the composite coating is the optimal at this moment. Subsequently, the corrosion rate of the composite coatings is slowly increased when the concentration of $Ce(NO_3)_3$ exceeds 0.10 g/L. That is caused by the change in the crystal structure of the composite coatings owing to the excessive $Ce(NO_3)_3$ concentration, which reduces the corrosion resistance of the composite coatings. It can be verified in Fig. 12 (b) that the trend of the effect of

different concentration of $Nd(NO_3)_3$ in the plating solution on the corrosion rate of the Ni-Mo-P composite coatings is consistent with Fig. 12 (a). In summary, the corrosion rate of the composite coatings would be significantly reduced by adding lower concentration of $Ce(NO_3)_3$ and $Nd(NO_3)_3$. For the contrast, the addition of 1.00 g/L $Nd(NO_3)_3$ to the plating solution has more remarkable effect on reducing the corrosion rate of the Ni-Mo-P composite coatings, which is about 0.681 $g/m^2 \cdot h$.
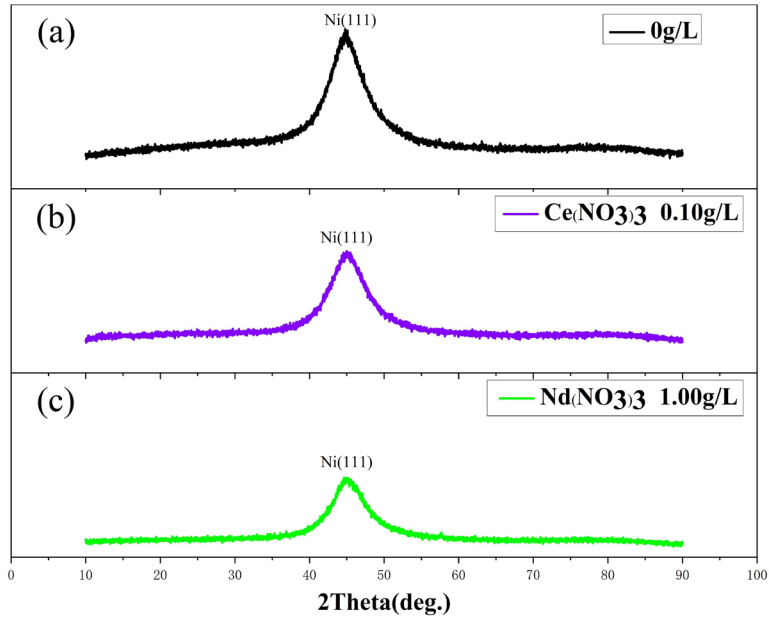
**Figure 8.** XRD patterns of Ni-Mo-P composite coatings.



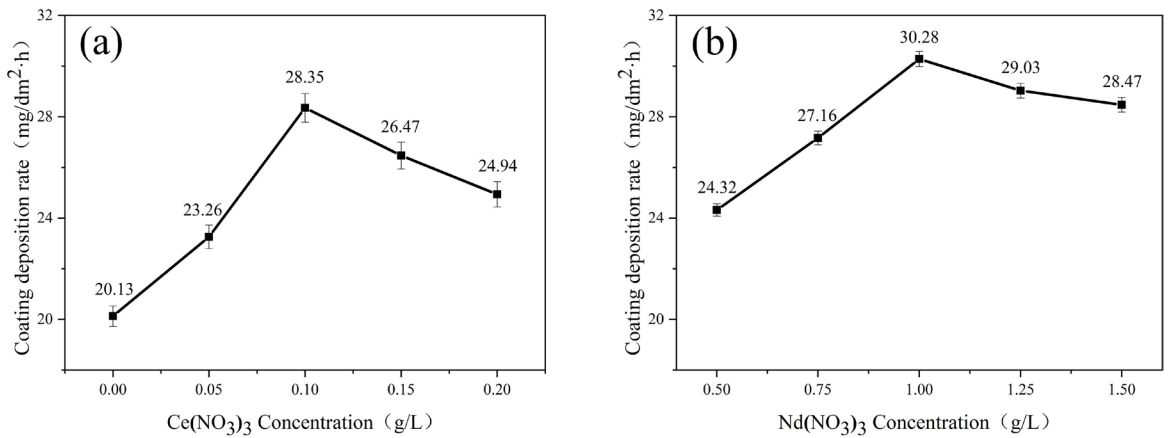**Figure 9.** Effect of the concentration of RE elements in plating solution on deposition rate (a) $Ce(NO_3)_3$ (b) $Nd(NO_3)_3$.

### 3.6.2. Effect of $Ce(NO_3)_3$ and $Nd(NO_3)_3$ concentration on the polarization curve of Ni-Mo-P composite coatings

The polarization curves of Ni-Mo-P composite coatings with different concentration of $Ce(NO_3)_3$ and $Nd(NO_3)_3$ in the plating solution are shown in Fig. 13. From Fig. 13 (a) that the corrosion potential ($E_{corr}$) of the composite coatings with different $Ce(NO_3)_3$ concentration are compared to the self-corrosion potential of the Ni-Mo-P composite coating which is about -0.58V, both have the certain improvement. Especially when the concentration of $Ce(NO_3)_3$ is 0.10 g/L, the composite coating has the optimal corrosion resistance and the maximum $E_{corr}$ is about -0.24 V. Fig. 12 (b) shows that with the addition of $Nd(NO_3)_3$ to the plating solution, the $E_{corr}$ of the composite coatings are all shifted to the right and the corrosion resistance is enhanced. When the

concentration of $Nd(NO_3)_3$ is 1.00 g/L, the maximum $E_{corr}$ of the composite coating is about -0.15 V, which is increase by 0.43 V compared with the $E_{corr}$ of the Ni-Mo-P composite coating. Herein, the Ni-Mo-P composite coating has the best corrosion resistance. Afterwards, the $E_{corr}$ of the composite coatings decreases with the concentration of $Nd(NO_3)_3$ exceeds 1.00 g/L, and the corrosion resistance is declined. This is mainly due to the composite coatings of the two plating solutions at the appropriate concentration is amorphous structure, and the corrosion-resistant passivation film generated on the surface is single-phase and uniform, which is not easy to form corrosion microcells.

In order to accurately investigate the corrosion resistance of the Ni-Mo-P composite coatings prepared with different concentration of $Ce(NO_3)_3$ and $Nd(NO_3)_3$, the data obtained after fitting to Fig. 13 are given in Table 5 and Table 6 in this study. By comparing the corrosion current

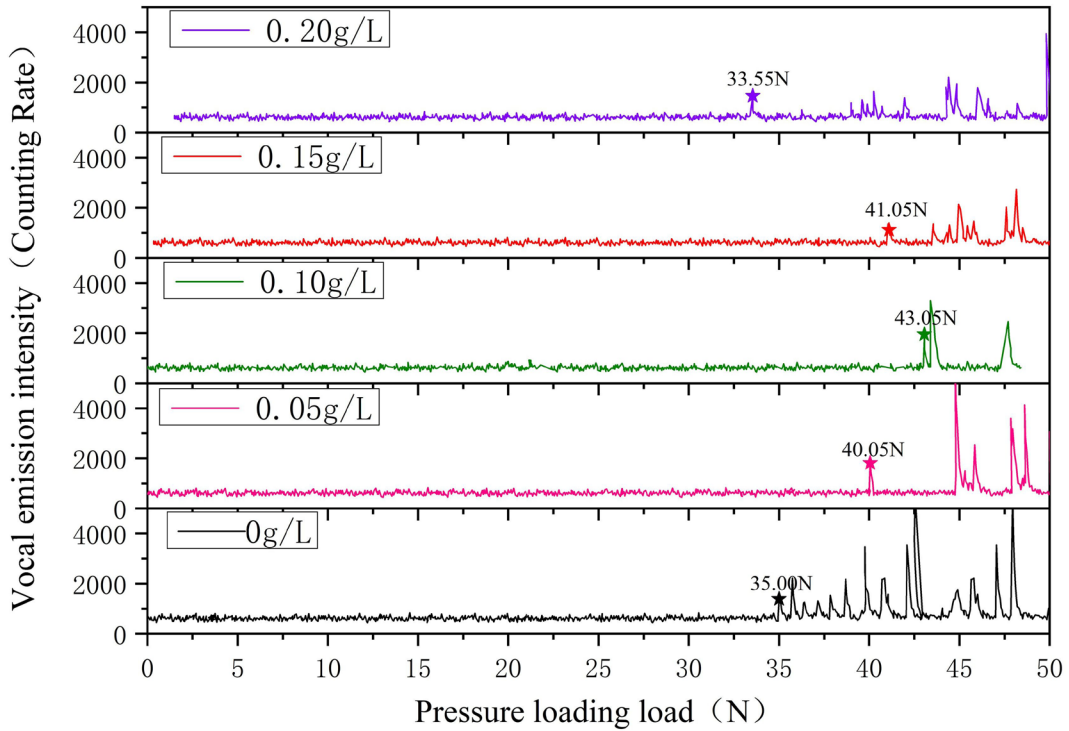**Figure 10.** Acoustic emission spectra of Ni-Mo-P composite coatings with different $Ce(NO_3)_3$ concentration.



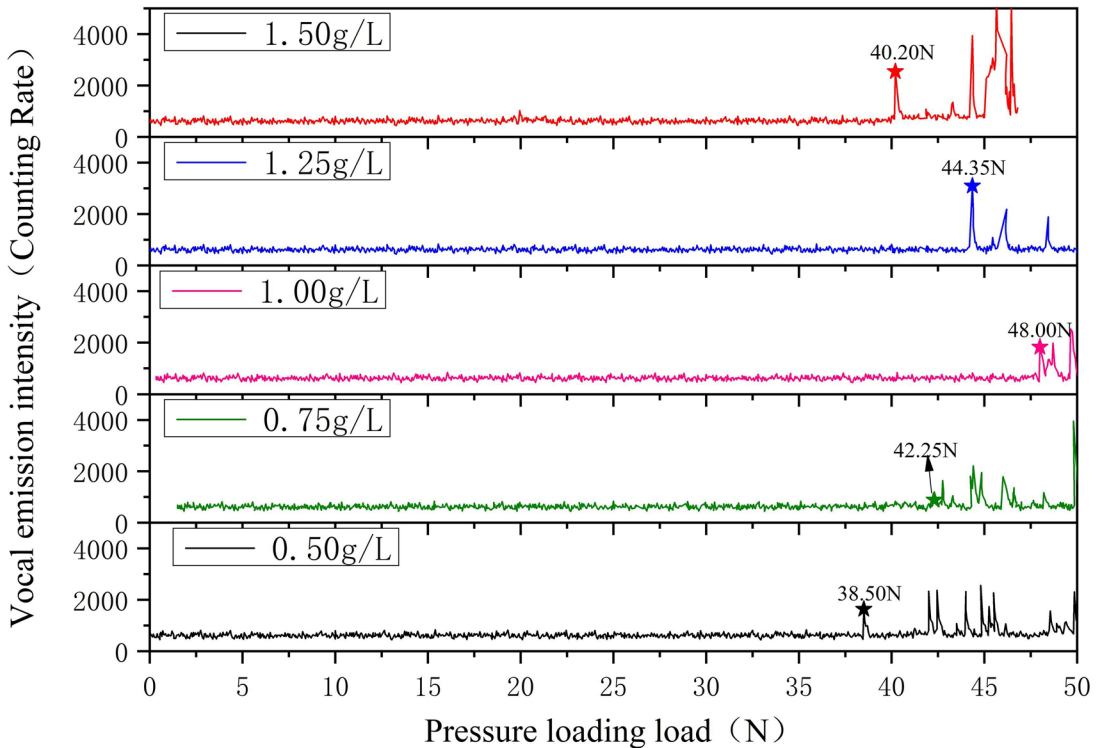**Figure 11.** Acoustic emission spectra of Ni-Mo-P composite coatings with different $Nd(NO_3)_3$ concentration.

density ($I_{corr}$) of different coatings in Table 5, it is know that as the concentration of $Ce(NO_3)_3$ increases from 0 g/L to 0.10 g/L, the $I_{corr}$ of the composite coatings decreases from $9.673 \times 10^{-3}$ A/cm² to $3.75 \times 10^{-4}$ A/cm², at which point

corrosion resistance is best. The corrosion resistance of the composite coatings gradually deteriorates due to the $Ce(NO_3)_3$ concentration exceeds 0.10 g/L. With the addition of $Nd(NO_3)_3$ to the plating solution, the $I_{corr}$ of the

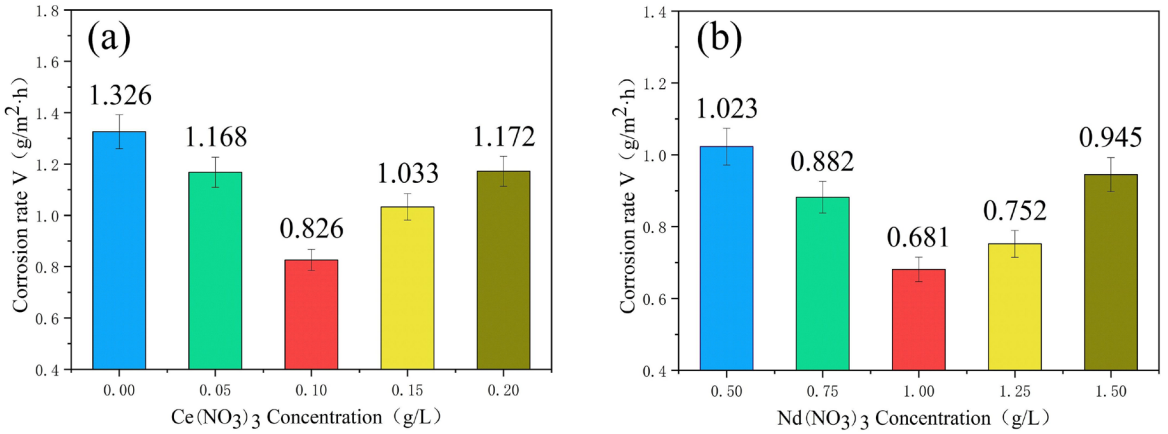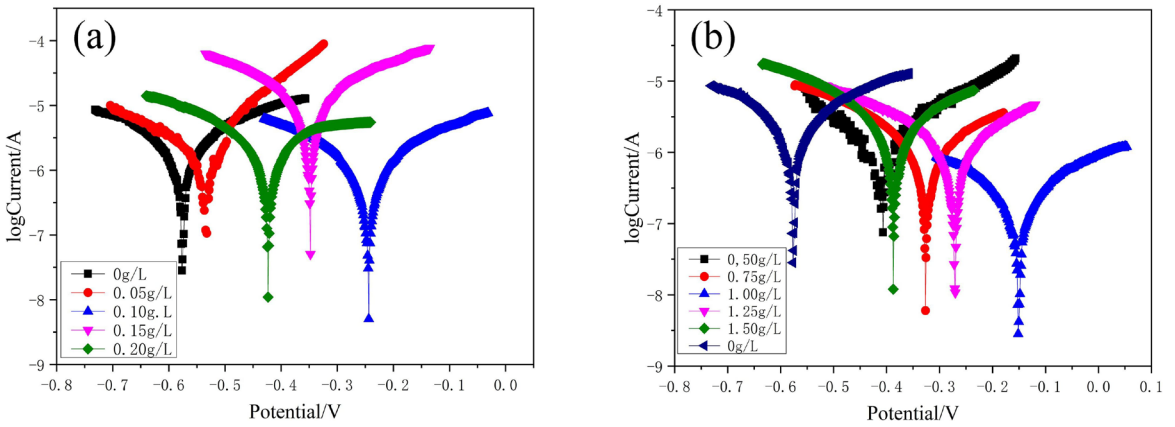**Figure 12.** Corrosion rate of Ni-Mo-P composite coatings with different concentration (a) $Ce(NO_3)_3$ (b) $Nd(NO_3)_3$.



**Figure 13.** Polarization curves of Ni-Mo-P composite coatings with different concentration (a) $Ce(NO_3)_3$ (b) $Nd(NO_3)_3$.

**Table 5.** Fitting parameters for polarization curves of Ni-Mo-P composite coatings with different $Ce(NO_3)_3$ concentration.

| $Ce(NO_3)_3$ (g/L) | $E_{corr}$(V) | $I_{corr}$(A/cm$^2$) |
|---|---|---|
| 0 | -0.58 | $9.673\times10^{-3}$ |
| 0.05 | -0.53 | $8.248\times10^{-3}$ |
| 0.10 | -0.24 | $3.75\times10^{-4}$ |
| 0.15 | -0.35 | $2.347\times10^{-3}$ |
| 0.20 | -0.42 | $6.324\times10^{-3}$ |

**Table 6.** Fitting parameters for polarization curves of Ni-Mo-P composite coatings with different $Nd(NO_3)_3$ concentration.

| $Nd(NO_3)_3$ (g/L) | $E_{corr}$(V) | $I_{corr}$(A/cm$^2$) |
|---|---|---|
| 0.50 | -0.41 | $6.154\times10^{-3}$ |
| 0.75 | -0.33 | $2.035\times10^{-3}$ |
| 1.00 | -0.15 | $7.3\times10^{-5}$ |
| 1.25 | -0.27 | $8.95\times10^{-4}$ |
| 1.50 | -0.38 | $4.032\times10^{-3}$ |

composite coating is reduced to different degrees, which is reflected in Table 6. The regularity of the $I_{corr}$ is opposite to the $E_{corr}$. The $I_{corr}$ of 1.00 g/L $Nd(NO_3)_3$ is the minimal, about $7.3\times10^{-5}$ A/cm$^2$ , which is two orders of magnitude lower than the $I_{corr}$ of Ni-Mo-P composite coating. This is related to its uniform and dense surface cytosol with fewer dislocations and other surface defects. The surface quality of the composite coatings and the thickness of the composite coatings under different concentration determine that the corrosion resistance effect of adding the suitable amount of $Ce(NO_3)_3$ is weaker than adding the suitable amount of $Nd(NO_3)_3$.

Experiments are performed with the untreated composite coating and four composite coatings with $Ce(NO_3)_3$ added to the EIS measurement plot displayed in Fig. 14. Fig. 14 (a) shows that the concentration of $Ce(NO_3)_3$ in the range of 0-0.10 g/L presents the trend of increasing the arc radius of capacitive and the corrosion resistance of the composite coatings gradually increases. With the increase of concentration, the arc radius of capacitive resistance starts to decrease at 0.15 g/L, and the arc radius of capacitive resistance decreases rapidly at 0.20 g/L. The corrosion resistance of the composite coatings decreases gradually during this period. Therefore, the corrosion resistance of the composite coating is optimal when the concentration of $Ce(NO_3)_3$ is 0.10 g/L. Demonstrate that the addition of appropriate amount of $Ce(NO_3)_3$ to the plating solution will enhance the corrosion resistance of the
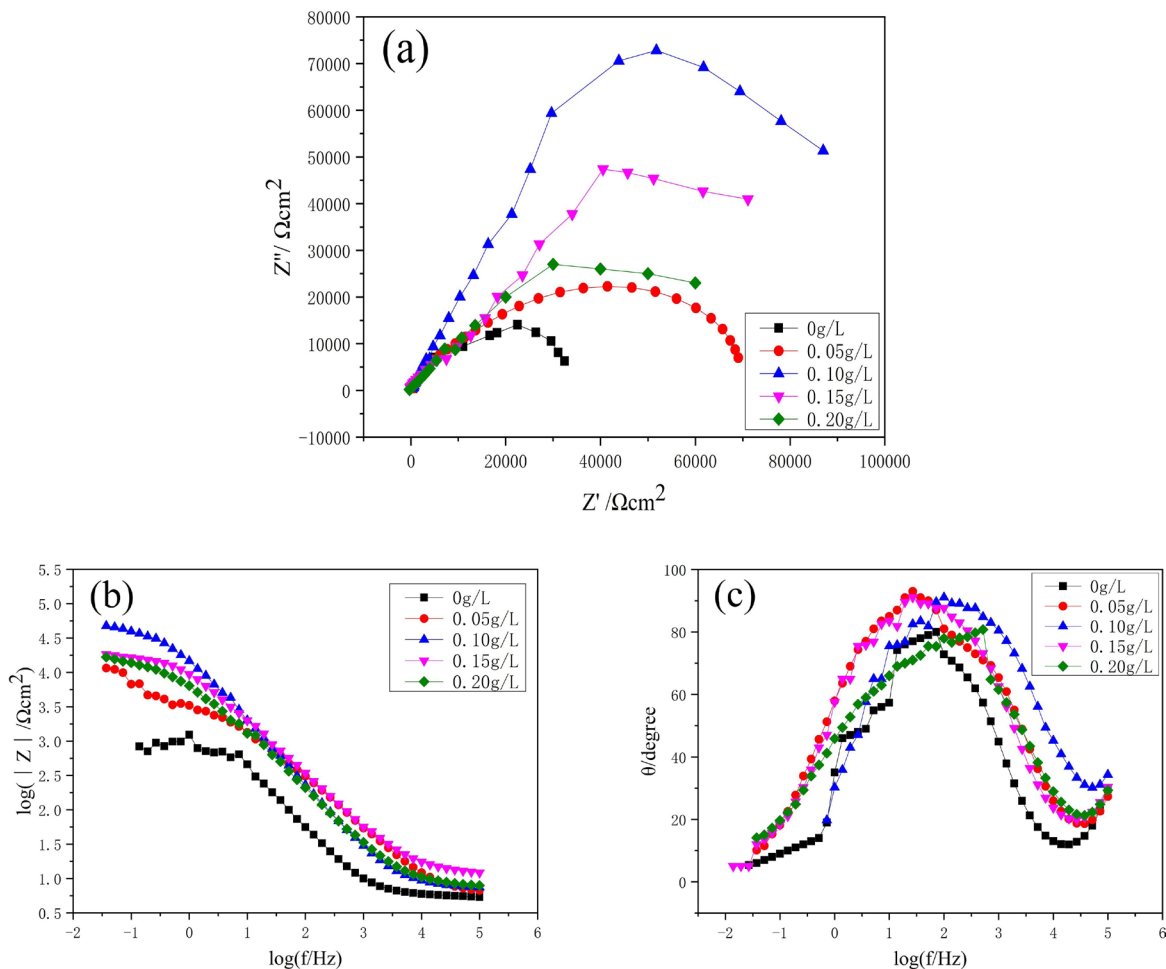
**Figure 14.** The Nyquist diagrams (a) and Bode diagrams (b-c) of Ni-Mo-P composite coatings with different Ce(NO$_3$)$_3$ concentration.

composite coatings. The above results are also verified in the Fig. 14 (b) and (c). In Fig. 14 (b), when the frequency range is within 1000 Hz-0.1 Hz, the impedance values of the added Ce(NO$_3$)$_3$ composite coatings are obviously increasing, and the impedance values are all higher than 4.0 at the highest point. In the phase angle diagram of Fig. 14 (c), the phase angle measured for the composite coatings tends to move toward the high frequency region as the concentration of Ce(NO$_3$)$_3$ in the plating solution increases. When the concentration is 0.10 g/L, the width of the narrow peak is the largest and the composite coating has the optimum protection effect on the substrate.

Fig. 15 shows the nyquist and bode diagram of the Ni-Mo-P composite coatings containing different concentration of Nd(NO$_3$)$_3$. Compared to the Ni-Mo-P composite coatings, the composite coatings obtained at Nd(NO$_3$)$_3$ concentration higher than 0.5 g/L shows a sign of increased capacitive arc resistance. When the concentration of Nd(NO$_3$)$_3$ is 1.00 g/L, the arc radius of capacitive resistance is the maximum and the Ni-Mo-P composite coating has the optimal corrosion resistance. Fig. 15 (b) reveals that when log f is less than 1, obviously the impedance value of the composite coatings with concentration higher than 0.75 g/L is still increasing, reaching the maximum value

of 4.75 at 1.00 g/L. While the impedance values of the composite coatings with Nd(NO$_3$)$_3$ concentrations of 0 g/L and 0.50 g/L are stable at 3.0 and 3.5, respectively. The Ni-Mo-P composite coatings in 3.5 wt.% NaCl solution with a single time constant is discernible in Fig. 15 (c), means that the Ni-Mo-P composite coatings prepared by adding Nd(NO$_3$)$_3$ to the plating solution can effectively prevent the contact between the corrosion solution and the magnesium alloy substrate. This coincides with the results given by the polarization curves.

The equivalent circuit diagram based on the electrochemical reaction principle is shown in Fig. 16. Form Fig. 16, Rs is the solution resistance, Rct is the charge transfer resistance, and Cdl is the double layer capacitance of the solution-metal interface before corrosion. The time constant of the electrochemical impedance spectrum is inferred to be 1 from the presence of a capacitive arc in the nyquist plots of Fig. 14 and Fig. 15, and verified that the electrochemical impedance spectrum has only one time constant from the corresponding bode diagram of a single hump. In other words, the NaCl solution only corroded the surface of the Ni-Mo-P composite coating and did not corrode the magnesium alloy substrate.
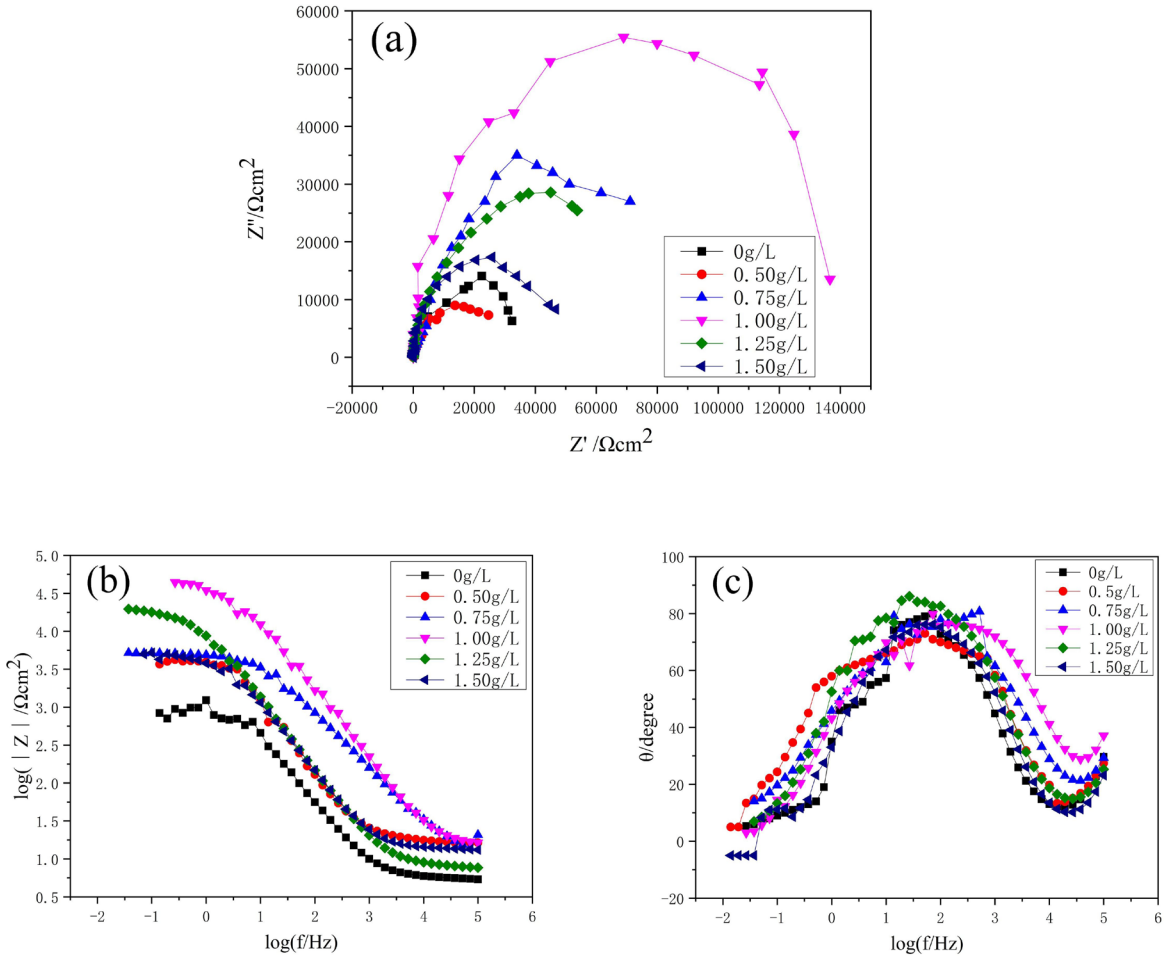
**Figure 15.** The Nyquist diagrams (a) and Bode diagrams (b-c) of Ni-Mo-P composite coatings with different Nd(NO$_3$)$_3$ concentration.



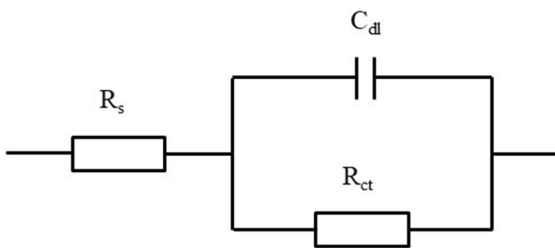**Figure 16.** Equivalent circuit model of Ni-Mo-P composite coating.

## 4. Conclusions

(1) Ni-Mo-P amorphous composite coatings containing Ce(NO$_3$)$_3$ and Nd(NO$_3$)$_3$ were successfully prepared on AZ91D magnesium alloy substrates by the proposed electroless plating method. By optimizing the concentration parameters, the Ni-Mo-P composite coatings with Ce(NO$_3$)$_3$ and Nd(NO$_3$)$_3$ reached the fastest deposition rates of 28.35 and 30.28 mg/dm$^2$·h, and the critical loads for coating damage reached 43.05 and 48.00 N, respectively.

(2) When the concentration of Ce(NO$_3$)$_3$ and Nd(NO$_3$)$_3$ were 0.10 g/L and 1.00 g/L, respectively, the minimum corrosion rate was about 0.826 and 0.681 g/m$^2$·h, the maximum self-corrosion potential was -0.24 and -0.15 V. Meanwhile, the arc radius of capacitive resistance in the impedance spectrum also maximum. In this case, the Ni-Mo-P composite coatings achieved the best protection of the substrate and the most excellent corrosion resistance.

(3) The performance of the composite coatings prepared at the optimum concentration of 0.10 g/L and 1.00 g/L for Ce(NO$_3$)$_3$ and Nd(NO$_3$)$_3$, respectively, especially the corrosion resistance, could be better obtained by adding Nd(NO$_3$)$_3$ to the plating solution than Ce(NO$_3$)$_3$.

## 5. Acknowledgments

# 6. References

1. Song JF, She J, Chen D, Pan FS. Latest research advances on magnesium and magnesium alloys worldwide. J Magnes Alloy. 2020;8(1):1-41.

2. Xu TC, Yang Y, Peng XD, Song JF, Pan FS. Overview of advancement and development trend on magnesium alloy. J Magnes Alloy. 2019;7(3):536-44.

3. Wang W, Han P, Peng P, Zhang T, Liu Q, Yuan SN, et al. Friction stir processing of magnesium alloys: a review. Chin Shu Hsueh Pao. 2020;33(1):43-57.

4. Pan HC, Kang R, Li JR, Xie HB, Zeng ZR, Huang QY, et al. Mechanistic investigation of a low-alloy Mg-Ca-based extrusion alloy with high strength-ductility synergy. Acta Mater. 2020;186:278-90.

5. Gusieva K, Davies CHJ, Scully JR, Birbilis N. Corrosion of magnesium alloys: the role of alloying. Int Mater Rev. 2015;60(3):169-94.

6. Zang DM, Zhu RW, Zhang W, Yu XQ, Lin L, Guo XL, et al. Corrosion-resistant superhydrophobic coatings on Mg alloy surfaces inspired by lotus seedpod. Adv Funct Mater. 2017;27(8):1605446.

7. Senthilvasan PA, Rangarajan M. Corrosion protection of mild steel by graphene-based films. Mater Res Express. 2018;5(8):085020.

8. Zhang G, Wu L, Tang AT, Chen XB, Ma YL, Long Y, et al. Growth behavior of MgAl-layered double hydroxide films by conversion of anodic films on magnesium alloy AZ31 and their corrosion protection. Appl Surf Sci. 2018;456:419-29.

9. Tang MQ, Feng ZQ, Wu XY, Wang W, Li G, Yan ZW, et al. Microarc oxidation coatings containing TiC and NbC on magnesium alloy. Surf Eng. 2019;36(11):1171-9.

10. Guo X, Withanage WK, Paudel JR, Eremeev G, Hannon F, Rimmer R, et al. Fabrication and radio frequency properties of 3-GHz SRF cavities coated with $MgB_2$. J Supercond Nov Magn. 2020;34(1):99-106.

11. Zhang YG, Sun WC, Ma M, Tian SS, Liu YW, Xiao Y. Effect of MoS2 concentration on microstructure and tribological behavior of electrophoretic-electrodeposited Ni-Co-Al2O3-MoS2 composites. Mat Res. 2020;23(5):e20200296.

12. Ma M, Sun WC, Zhang YG, Liu YW, Dong YR, Zi JY, et al. Effect of TiC particles concentration on microstructure and properties of Ni-TiC composite coatings. Mater Res. 2019;22(6):e20190530.

13. Tian XX, Sun WC, Liu YW, Jia YP, Xiao Y. Effects of Na2WO4 concentration on the microstructure and corrosion behavior of Ni-W-P ternary coatings. Rare Materials Research. 2021;24(4):e20200580.

14. Wasserbauer J, Buchtik M, Tkacz J, Fintova S, Minda J, Doskocil L. Improvement of AZ91 alloy corrosion properties by duplex Ni-P coating deposition. Materials. 2020;13(6):1357.

15. Zhang J, Song ZW, Yu G, Hu BN, Zhang XY. Corrosion behavior of electroless Ni-P/Ni-B coating on magnesium alloy AZ91D in NaCl environment. Int J Electrochem Sci. 2016;11(12):10053-66.

16. Buchtik M, Kosar P, Wasserbauer J, Tkacz J, Dolezal P. Characterization of electroless Ni-P coating prepared on a wrought ZE10 magnesium alloy. Coatings. 2018;8(3):96.

17. Zhou P, Cai WB, Yang YB, Li XJ, Zhang T, Wang FH. Effect of ultrasonic agitation during the activation process on the microstructure and corrosion resistance of electroless Ni-W-P coatings on AZ91D magnesium alloy. Surf Coat Tech. 2019;374:103-15.

18. Wang WC, Ju X, Xu CY, Zhang WW, Mitsuzaki N, Chen ZD. Study on electroless plating Ni-W-P ternary alloy with high tungsten from compound complexant bath. J Mater Eng Perform. 2020;29(12):8213-20.

19. Chen J, Zhao GL, Matsuda K, Zou Y. Microstructure evolution and corrosion resistance of Ni-Cu-P amorphous coating during crystallization process. Appl Surf Sci. 2019;484:835-44.

20. Ariffah MSN, Nurulakmal MS, Anasyida AS, Shiu EK. Surface roughness, wear and thermal conductivity of ternary electroless Ni-Ag-P coating on copper substrate. Mater Res Express. 2020;7(2):026536.

21. Zhang Q, Ning LP, Wang CY, Wang M, Shen YZ, Yan YR. Fabrication and characterization of bio-based shielding material with dissimilar surface resistivity prepared by electroless Ni-Fe-P alloy plating on bamboo (N. affinis). J Mater Sci Mater Electron. 2019;30(24):21064-78.

22. Wang YR, Tang RJ, Yang CH, Xu TY, Mitsuzaki N, Chen ZD. Effect of sodium stannate on low temperature electroless Ni-Sn-P deposition and the study of its mechanism. Thin Solid Films. 2019;669:72-9.

23. Jiang JB, Chen HT, Wang YH, Zhu LY, Sun YX, Lin HL, et al. Effect of ultrasonication and $Na_2MoO_4$ content on properties of electroless Ni-Mo-P coatings. Surf Eng. 2018;35(10):873-82.

24. Sarkar S, Baranwal RK, Biswas C, Majumdar G, Haider J. Optimization of process parameters for electroless Ni-Co-P coating deposition to maximize micro-hardness. Mater Res Express. 2019;6(4):046415.

25. Armyanov S, Valova E, Tatchev D, Georgieva J. Electroless deposited ternary alloys: third element chemical state, localisation and influence on the properties. a short review. Trans Inst Met. 2018;96(1):12-9.

26. Balaraju JN, Raman N, Manikandanath NT. Nanocrystalline electroless nickel poly-alloy deposition: incorporation of W and Mo. Trans Inst Met. 2014;92(3):169-176.

27. Gao Y, Wang JH, Yuan J, Li HQ. Preparation and magnetic properties of Ni-P-La coating by electroless plating on silicon substrate. Appl Surf Sci. 2016;364:740-6.

28. Wang ZH, Zhang LL, Ni H, Wang SJ. Effects of $Y^{3+}$ on properties of electroless NiYP coatings. Surf Eng. 2016;32(5):385-90.

29. Bi SY, Zhao H, Hou L, Lu YX. Enhanced electromagnetic interference Shielding effects of Cobalt-Nickel polyalloy coated fabrics with assistance of rare earth elements. Fibers Polym. 2018;19(5):1084-93.

30. Song YL, Liu YH, Wang SH, Yu SR, Zhu XY. Effect of cerium addition on microstructure and corrosion resistance of die cast AZ91 magnesium alloy. Materials and Corrosion. 2007;58(3):189-92.

31. Zhao DZ, Zhang DF, Liu YP, Hu GS, Gou YN, Pan FS. Neodymium-based conversion coating on AZ31 magnesium alloy. Rare Metal Mat Eng. 2017;46(2):289-95.

32. Han BJ, Gu DG, He Q, Zhang XL, Peng GH, Yang CB. Fabrication of a novel Mg-RE (Nd, Ce) intermetallic compound coating by molten salt diffusion and its effect on corrosion resistance of magnesium alloys. J Rare Earths. 2016;34(7):731-5.